Journal of Materials Processing Tech. 310 (2022) 117758

Contents lists available at ScienceDirect

Journal of Materials Processing Tech.

journal homepage: www.elsevier.com/locate/jmatprotec

Acoustic emission monitoring for necking in sheet metal forming

Madhav Baral [a,*], Ali Al-Jewad [b], Alexander Breunig [c], Peter Groche [c], Jinjin Ha [b], Yannis P. Korkolis [d], Brad L. Kinsey [b]

[a] Department of Mechanical and Aerospace Engineering, University of Kentucky, Lexington, KY 40506, USA
[b] Department of Mechanical Engineering, University of New Hampshire, Durham, NH 03824, USA
[c] Institute for Production Engineering and Forming Machines, Technische Universität Darmstadt, Darmstadt, Germany
[d] Department of Integrated Systems Engineering, The Ohio State University, Columbus, OH 43210, USA

ARTICLE INFO

Associate Editor: Marion Merklein

Keywords:
Acoustic emission
Source triangulation
Uniaxial tension
Cup drawing
Localization
Necking

ABSTRACT

There is extensive evidence in the literature that plastic deformation of metals is associated with an increase in Acoustic Emission (AE) activity. Thus, AE measurement techniques have the potential to monitor a forming process in real time and provide a signal for feedback control, to exploit optimum formability. In this work, custom-made AE sensors employing piezoelectric crystals are implemented to measure the emitted acoustic signal during uniaxial tension and cup drawing tests of an AA6013-T4 aluminum sheet (1.5 mm thick). The uniaxial tension tests are conducted with two AE sensors clamped to each end of the specimen gage section, along with full-field surface strain measurement using Digital Image Correlation (DIC) techniques. The AE signals along with the interrogation of the DIC images reveal that the maximum AE amplitude corresponds to the onset of diffuse necking, i.e., when the strain field starts to become spatially inhomogeneous. Interestingly, this onset occurs before the maximum force is attained. Comparing these observations to a model of dislocation activity supports the notion that dislocation is the main driver of AE activity. With these findings, AE measurements are performed in a cup drawing process where a custom-made Marciniak-type punch incorporates three AE sensors. These sensors are used to triangulate and determine the location of necking and eminent fracture based on the time difference of arriving signals to each sensor. The results from the cup drawing tests show that AE signals can identify the onset of necking and accurately predict the location of necking and fracture.

1. Introduction

The ASTM E1316 standard outlines Acoustic Emission (AE) as “the class of phenomena whereby transient elastic waves are generated by the rapid release of energy from localized sources within a material, or the transient elastic waves so generated" (Kawamoto and Williams, 2002). AE measurement is a technique to detect those elastic waves; an AE signal can be used as a diagnostic tool for the condition of the material, including avoiding failure during manufacturing processing.

As a material deforms, it emits elastic waves due to the changes in the internal structure (Behrens et al., 2011). Studies with crystalline materials have suggested that these waves are caused during plastic deformation by sudden localized and irreversible microstructural changes. However, researchers debate over the exact phenomena that are responsible for the elastic waves, making it hard to identify a single source for AE signals. Carpenter and Higgins (1977) and Heiple and Carpenter (1987) summarized some of the sources of mechanisms responsible for generation of AE during plastic deformation, that include dislocation glide, twinning, Lüder’s band formation, slip-line formation, dislocation breakaway, and dislocation multiplication. The other possible sources mentioned in literature include microcrack formation (Schofield, 1958), changes in mobile dislocation density (Dunegan and Harris, 1969), slip advances (Fisher and Lally, 1967), and alternate slip-on transient planes (Fitzgerald, 2005). In addition, Barschdorff and Haupt (2000) mentioned anisotropies, phase transformations, and martensite formation as other likely sources of AE. The increase in AE activity has been correlated to the increase in the dislocation density within a given material (Khalil, 2011). Furthermore, working with 7075 Aluminum, Dunegan and Harris (1969) successfully correlated the AE signal as a function of plastic strain to the evolving dislocation density using Gilman (1966) model. Gilman’s model has also been applied to the current work and is discussed in a later section.

Typical AE signals have been classified into two types: continuous and burst signals (Luis and Chacon, 2015). A burst signal is one that has

* Corresponding author.
E-mail address: madhav.baral@uky.edu (M. Baral).

https://doi.org/10.1016/j.jmatprotec.2022.117758
Received 7 June 2022; Received in revised form 3 August 2022; Accepted 19 August 2022
Available online 23 August 2022

identifiable changes at the beginning and end (Huang, 2013). Typically, it has little information and slight change over most of the observation time window, except for a short fraction of the time where most of the information "bursts" out. Continuous AE is created by a series of overlapped pulse-type signal components (Barschdorff and Haupt, 2000). The processing of a burst signal is different from that of a continuous signal, as the sampling of the burst needs to capture the fast variation over the shortest period possible.

Even if the source of the AE signal might be unclear, this signal can still be utilized in various ways (Vanniamparambil et al., 2015). AE is a widely used nondestructive testing (NDT) technique in many disciplines, e.g., in materials processing (Calabrese and Proverbio, 2020) and in civil engineering as mentioned in Nair and Cai (2010), for evaluating structural defects. Huang et al. (1998) highlighted the major advantage of AE technique over other NDT such as ultrasound and x-ray, as the former detects the activities inside the materials, while the latter attempts to examine the internal structures of the materials. Thus, using AE, the structure or specimen being examined can be subjected to the in-service or laboratory operation while the other NDT often requires structure or specimen to be disassembled and taken to the laboratory to be examined.

Focusing on manufacturing applications, the experimental results from Liang and Dornfeld (1990) suggested that there is a relationship between AE energy and metal forming process states. In that study, the AE signal was utilized in characterizing the material deformation during stretching and deep drawing. Moreover, Skåre et al. (1998) utilized the AE signal to give information about the friction and the forming processes between two surfaces in contact like tool and workpiece in deep drawing. This was used to supervise the behavior of the two by means of AE monitoring to identify multiple process events such as galling, cracks, and tool wear. Hao et al. (2000) ran a test program which addressed the issues of AE transducer characterization, the propagation of AE through a plastically-deforming material and the monitoring of AE-deformation in sheet metal forming. More recently, Behrens et al. (2011) studied the feasibility of using AE signals for real time monitoring of deep drawing processes. In their study, they concluded that the AE signal proved its suitability for the purpose of general material characterization and failure analysis. They showed how to detect and analyze deep drawing defects like cracking and wrinkling or other disturbing process faults like insufficient lubrication or incorrect positioning of blanks. They characterized changes in the AE activity associated with varying blank holder force, lubrication conditions, and the position of the blanks.

One of the common reasons of punch press failure is due to tooling failure. Thus, the ability to predict or monitor the tool wear before it leads to complete failure is crucial in manufacturing processes. To that end, Kim (1983a, 1983b) divided the AE signal emitted from a punch press into three parts depending on the relative time of their occurence and amplitude. Those parts were shown to have certain charactreistic features and were labeled initial impact, shear fracture and rupture. The parts were then perfectly correlated with the stock hardness, stock thickness, tool size and tool wear. The conclusion made was that the AE signal can be used to develop a reliable monitoring system for high speed punch presses in real time to prevent tool failure by an early detection of abnormal operating conditions. Likewise, Jemielniak and Otman (1998) applied the AE measurement in metal cutting to in-process detection of catastrophic tool failure using statistical analysis of the distribution of the AE root mean square signal. In another study performed by Nakao and Dornfeld (2003), the AE signal was actually utilized in designing a feedback control system for diamond turning that reduced machining error by 20%.

From the works reported above, it can be claimed that AE measurements can provide useful feedback for manufacturing process control and such an idea is shared among researchers. Mokbel and Maksoud (2000) used AE technique to monitor the condition of diamond grinding wheels by imprinting the surface profile of the wheel onto mild steel specimens, concluding that AE technique can be a useful tool in monitoring the grinding process. Jayakumar et al. (2005) reviewed on-line monitoring of various forming processes such as punch stretching, drawing, blanking, forging, machining and grinding, and concluded AE technique being the important and advanced nondestructive evaluation tools that has the capabilities for real time process monitoring application. Gupta et al. (2021) reported that AE technique has more favorable advantages of quick and overall testing by means of multiple sensors, high sensitivity, sensor mounting for process control and no requirement of disassembling and sample cleaning.

Furthermore, determining the onset of localized necking and creating the Forming Limit Curve (FLC) facilitates sheet formability assessment and is of great interest to the forming industry. Nowadays, Digital Image Correlation (DIC) techniques are widely used to determine the onset of localized necking to improve the accuracy of FLC's. Vacher et al. (1999) analyzed the strain increments between successive images of a forming process to estimate the onset of localized necking. Wang et al. (2014) proposed a method to identify the onset of localized necking based on analysis of the changes of surface topography of the specimen (i.e., changes in specimen thickness). Martínez-Donaire et al. (2014) used DIC techniques to compute the displacement and strain evolutions at the outer surface of the tested specimens, and analyzed two physically-based methodologies, categorized as a time-dependent method and a time-position-dependent method, in detail to assess the failure by necking. Likewise, Min et al. (2017) conducted Marciniak tests incorporating DIC measurements to propose a method based on surface curvature change to detect the onset of localized necking for in-plane deformation. Ha et al. (2020) proposed a radically different approach to FLC determination, by taking advantage of the noise inherent in DIC strain measurements, and its 1st and 2nd derivatives.

In this work, we employ AE sensors to obtain the emitted signal from a uniaxial tension (UT) test and a cup drawing test of the aluminum alloy AA6013-T4 to monitor the plastic deformation process. Though AE is a phenomenon resulting from microstructural activity, the focus of this study is on correlating the AE measurements on the macroscopic behavior of the material. Of particular interest is the detection of necking that leads to fracture, thus controlling the forming limits. Section 2 describes UT tests that utilize both AE sensors and 2-D DIC for the surface strains. By correlating the AE information to strain, an early detection of diffuse necking, prior to the force maximum, is observed. Section 3 discusses a cup drawing test where three AE sensors are embedded in a Marciniak-type punch to triangulate the necking location where fracture occurs. The AE measurements are correlated with DIC strain results, as before. Section 4 discusses the results in the context of their application for forming control, and also offers a possible explanation of the AE activity recorded. The paper concludes with Section 5, which describes future applications of this work in forming. For the first time, an AE technique is utilized in this work to observe diffuse neck formation before the maximum force is attained. It also establishes dislocation density evolution as the cause of AE activity. On the forming side, it is demonstrated for the first time that the location and instance of necking can be pin-pointed, in real time. This can inform a closed-loop control of the forming process, to avoid failure. The ongoing goal of this research is to use the knowledge obtained to detect the onset of necking during forming, and to integrate it into a closed-loop control system to adjust the process parameters and increase formability in sheet metal forming.

2. Uniaxial tension

2.1. Material and specimen preparation

The material used in this study is a 1.5 mm thick cold-rolled aluminum sheet in the T4 temper, AA6013-T4. The nominal composition of this material is shown in Table 1 (Berneder et al., 2011). The plasticity and fracture of this alloy (with a sheet thickness of 2 mm) was

Table 1
Chemical composition of AA6013-T4 sheet (wt%).

Al	Cu	Fe	Mg	Mn	Si	Cr	Zn
95.05–96.95	0.6–1.1	< 0.5	0.8–1.2	0.2–0.8	0.6–1.0	< 0.1	< 0.25

characterized in an earlier work (Ha et al., 2018). The specimens for the uniaxial tension (UT) tests are prepared using a waterjet cutting process and were sanded afterward to achieve a finer surface finish. The ASTM E8 specimen geometry is used for the UT tests. A typical stress-strain curve in the rolling direction (RD) is shown in Fig. 1, with a yield stress at 0.2% offset strain of 289.6 MPa, ultimate tensile stress of 349.7 MPa, and fracture strain of 24.4%.

2.2. Experimental setup

The UT tests are performed on an MTS Landmark 370 servo-hydraulic testing machine of 250 kN load and 176 mm stroke capacity, which is equipped with FlexTest software and controller, and hydraulic grips. The tests are performed at room temperature at a cross-head velocity of 6.1 mm/s, which induces the relatively high nominal strain-rate of 1.22×10^{-1} /s in the gage-section. The experimental setup for the UT test, along with MTS grips, is shown in Fig. 2. The AE sensors are clamped on the specimen using insulated binder clips, as seen in the inset of Fig. 2, to prevent an electrical short-circuiting between the binder and sensor. Glycerin is applied as a couplant between the sensors and the specimen surface, to facilitate transmission of elastic waves generated during the plastic deformation. The two AE sensors are positioned 50 mm apart on the specimen, along the gage length, with the 10 mm long grids marked on the specimen surface, as seen in the inset of Fig. 2. During the tests, the force signal from the MTS machine and AE signals from the AE sensors are recorded at the same time in the digital oscilloscope. The DIC images from the test are also collected separately in the DIC computer and synchronized manually with the rest of the signals.

2.3. Acoustic emission sensors

The AE measurements in this work are obtained using a custom-made sensor employing piezoelectric crystals from APC International. The disk-shaped sensor has a diameter of 9.5 mm and thickness of 3.9 mm with a side tab silver electrode pattern, to which wires from both positive and negative electrodes are soldered (see sensor image at top left of Fig. 3). Note that one surface of the crystal is kept wire-free by attaching the wire at the tab on the lateral side of the crystal. This allows

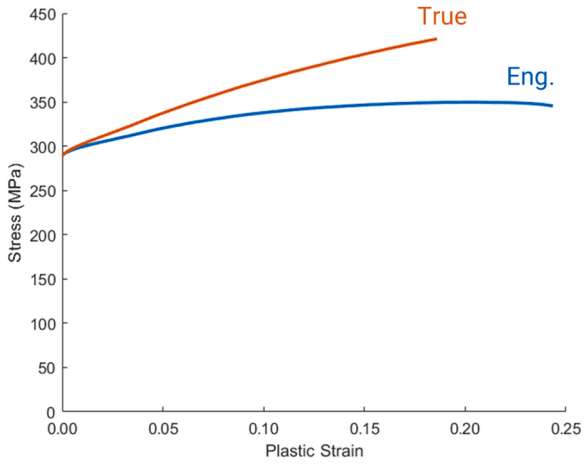

Fig. 1. – Stress-strain curves from a UT test in RD.

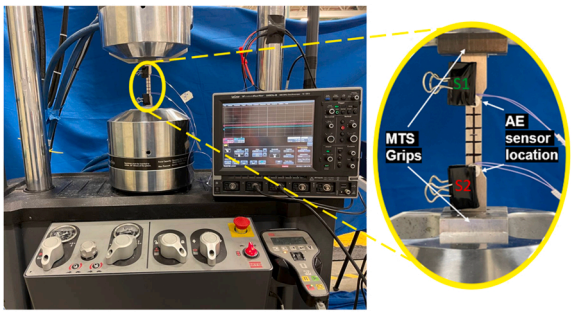

Fig. 2. – Experimental setup for a UT test showing MTS grips and AE sensors clamped on the specimen.

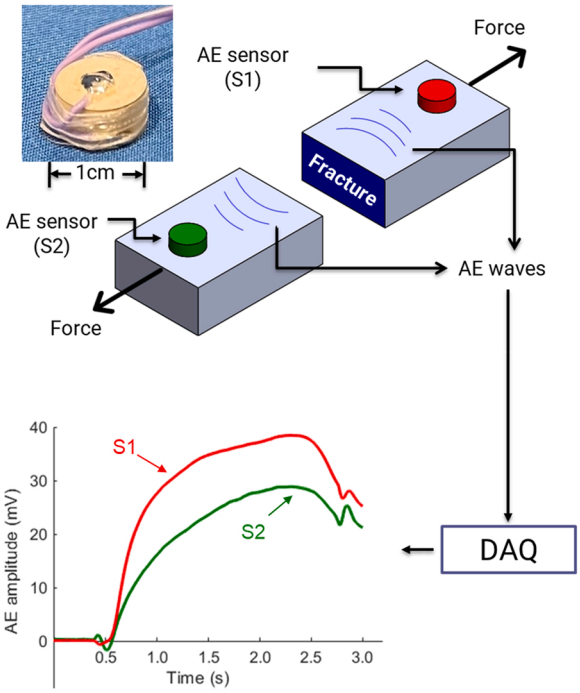

Fig. 3. – Schematic of the AE system showing sensors, DAQ, and AE signals.

direct contact of the sensor with the sheet metal, so that AE signals can be transmitted during the deformation. The frequency response behavior of the piezoelectric crystal, as supplied by the manufacturer, has a resonance frequency around 520 kHz. The use of home-made sensors enabled the use of existing data-acquisition hardware and thus lowered the cost of the tests.

2.4. Data acquisition and signal processing

The AE signals detected by the sensors during the tests are recorded using a digital oscilloscope (Teledyne Lecroy WaveSurfer 64MXs-B) with 600 MHz bandwidth, 4 digital channels, and a sampling rate up to 10 GS/s. The system is set to single trigger mode in every test, and data is logged once the signal crosses the threshold set by the user (~0.2 mV). The AE data during the UT tests are sampled at 20 kHz. This low sampling rate is sufficient to monitor the signal amplitude as opposed to capturing the entire AE waveform, which typically requires a high sampling rate in the order of MHz. A simplified schematic of the AE system, including the data acquisition (DAQ) device, is shown in in Fig. 3.

A typical AE signal recorded by an AE sensor during a UT test is shown in Fig. 4. The signal recorded is continuous from prior to the onset

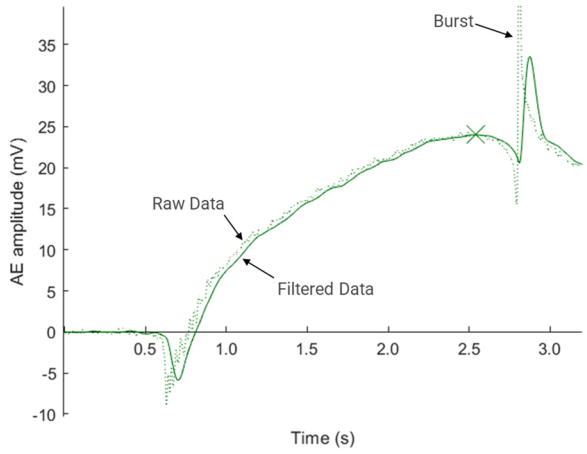

Fig. 4. – A typical AE signal obtained during a UT test shown along with raw and filtered data.

of plastic deformation until after fracture, which is typically seen as a burst peak (see Fig. 4). As the plastic deformation increases, the AE signal from each sensor increases until it reaches a maximum (marked as "x" in Fig. 4). Then, the signal decreases until the specimen fractures. This phenomenon is repeatedly observed in additional tests.

The raw AE signal is transformed into the frequency domain using a Fast Fourier Transform in MATLAB. This transformation converts a signal into individual spectral components and provides frequency information about the signal and the noise. This information is used to design a digital filter. A low pass filter that has a frequency response as flat as possible in the passband is desired to preserve the observed characteristics of the curve. A Butterworth filter (Selesnick and Sidney Burrus, 1998) of third order and with a 7 Hz bandwidth is implemented to smooth the measured raw AE signals. A MATLAB function "butter.m" is implemented to return the transfer function coefficients of the third order lowpass filter with a normalized cutoff frequency of 7 Hz. Then, the raw AE signals are passed through the filter to get the smoothed responses. The filtered data along with the raw data from a UT test are shown in Fig. 4. Note the lag in the filtered data, as expected for Butterworth filters. As discussed in Section 4, this has limited impact on our final observations.

2.5. Digital Image Correlation

Concurrently with the AE measurements, the full-field strain of the uniaxial tension test is acquired using the 2-D DIC method (Sharpe, 2009; Shukla and Dally, 2010). The VIC-Snap system (Correlated Solutions Inc.) is used to acquire the images from one 2.0 Megapixel digital camera equipped with a 35 mm Schneider lens. An image frame is recorded every 100 ms during the test. The images are then post-processed using the VIC-2D software with a subset size of 29 pixels, a step size of 7 pixels, and a filter size of 5.

2.6. Results and discussion

A UT test result showing the AE signals from the two sensors and force data is shown in Fig. 5a. The failed specimen from this test is shown in Fig. 5b. The fracture location is 13 mm below the center within the gage section, as marked with a red X in Fig. 5b. The AE signals shown in Fig. 5a are smoothed as described in Section 2.3. Note, the force signal is not subjected to the digital filter, thus it does not have the lag observed in AE signals shown in Fig. 4. The maximum amplitudes from the AE signals prior to fracture for each sensor and the maximum force value are all marked as "x" in Fig. 5a. The fracture of the specimen corresponds to the sudden drop of the force to zero, and abrupt peaks, i.e., smoothed burst events, in the AE signals. The maximum peaks in the AE-time

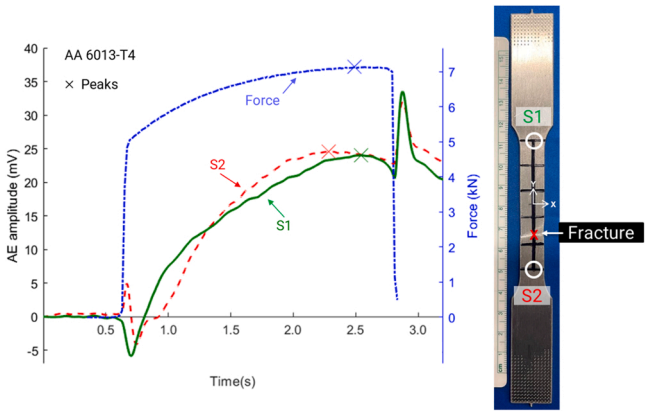

Fig. 5. – (a) UT test result showing AE signals and force data and (b) the corresponding failed specimen.

curves occur before the force maximum and correspond to the early onset of diffuse necking or when the strain field starts to become inhomogeneous due to localization effects. This phenomenon has been observed repeatedly in this work and will be discussed in detail later in this section. Note that the smoothing of the AE signals (see Fig. 4) with the low pass filter shifts the curves forward in time. Thus, the peaks in the AE signals actually occur even earlier before the UTS of the material.

The AE peak velocity can be determined by knowing the location of the neck and the time difference between the AE peaks from the two sensors. From Fig. 5a, the time difference, Δt, is 0.2275 s. From Fig. 5b, the distance between the center of the specimen and the fracture location, Δx, is measured to be 13 mm. Based on this information, the AE peak velocity is determined as $v = (2\Delta x)/\Delta t = 114.3$ mm/s. As seen in Fig. 5b, the fracture location is closer to Sensor 2 than Sensor 1. Thus, when the wave propagates, the maximum peak of the AE signal from Sensor 2 is recorded earlier than that from Sensor 1, as seen in Fig. 5a. Similar findings are observed in repeated UT tests with the average AE peak velocity (from 6 tests) being around 115 mm/s. This AE peak velocity will be used in predicting the fracture location for cup drawing tests described in Section 3. Also, it is worth noting that the average velocity of sound waves in aluminum is around 6420 m/s. This difference in velocities indicates that the AE peak speed is possibly a phenomenon tied to the dislocation speed rather than the actual elastic wave speed. However, this needs to be justified with further investigations.

As mentioned earlier in this section, it is important to investigate the AE peaks to determine if these indeed correspond to the early onset of necking. This is achieved by evaluating the strain data from the DIC

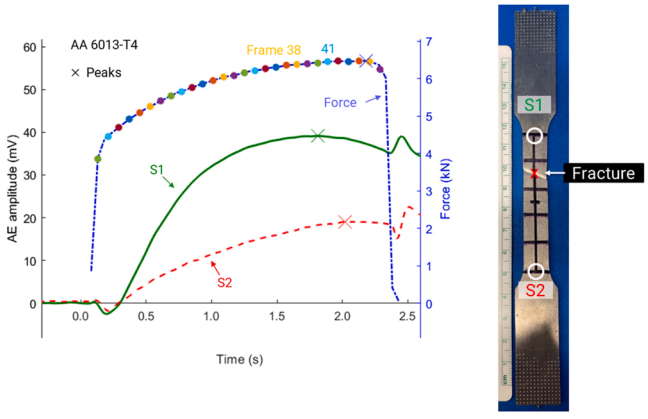

Fig. 6. – (a) Second UT test result showing AE signals, force data, and DIC frame numbers and (b) the corresponding failed specimen.

method described in Section 2.3. A second UT test with a DIC image acquisition of 12 fps is shown in Fig. 6a with a failed specimen image shown in Fig. 6b. The maximum force and the maximum AE amplitudes from both sensors are marked on the corresponding curves. In this test, the necking and fracture occurs at 13 mm above the center of the specimen, as shown in Fig. 6b. From Fig. 6a, the time difference between two sensors, Δt, is 0.211 s. In this test, the AE peak velocity is calculated to be 123.2 mm/s, reasonably consistent with previous findings. The true strain fields on the surface from the DIC are shown in Fig. 7, corresponding to Frames 38 – 41, which are also marked in the force-time curve in Fig. 6a. As shown in Fig. 7, the strain field starts to transition from homogenous to non-homogenous state between Frame 38 (= 14.49% nominal strain) and Frame 41 (= 16.74%). As the strain non-uniformity becomes more pronounced, the AE signals reach their maximum values as seen in Fig. 6a. The AE peaks are found to occur before the force peak (i.e., the ultimate stress, conventionally associated with the onset of necking, to 1st order) and can be attributed to the strain field transitioning from spatially uniform to non-uniform just before the strain localization. Assuming that the dominant source of the AE signal is dislocation motion, diffuse necking implies that only a small region continues to deform plastically, while the rest of the specimen unloads elastically, yielding a reduction in the overall AE activity inside the specimen. Note that another material was investigated, i.e., DP 780, and showed similar effects but is not presented here for conciseness.

This finding can be further substantiated by additional interrogations of the DIC images in terms of strains and strain-rates. The evolution of axial strain is shown in Fig. 8 by probing the strains across a normalized length (i.e., white dashed line shown in Frame 38 of Fig. 7) at increasing levels of deformation. As seen in the figure, the solid curves represent the axial strains extracted from points along the normalized gage length and dashed lines represent the average of the corresponding solid curves. The strains remain uniform until Frame 38 and start to transition towards non-uniformity until Frame 41, with a pronounced necking seen at later frames. This strain evolution along with the force-time curve is shown in a three-dimensional plot in Fig. 9, where the non-uniformity in the strain is seen to occur before the force maximum.

The above findings indicate some evidence of an early onset of a diffuse neck while the force signal is still increasing. Classically, it is considered that the diffuse neck occurs when the force reaches its maximum (Considère, 1885). Further analytical studies predicted the onset of necking past the max. force as shown by (Hill and Hutchinson, 1975) and (Hutchinson and Miles, 1974). However, it is not uncommon

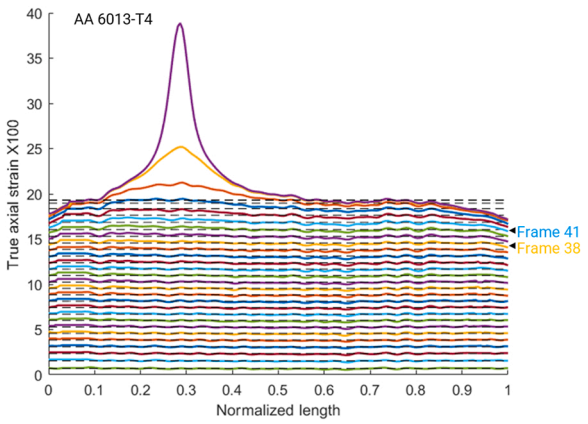

Fig. 8. – Evolution of axial strain during the UT test.

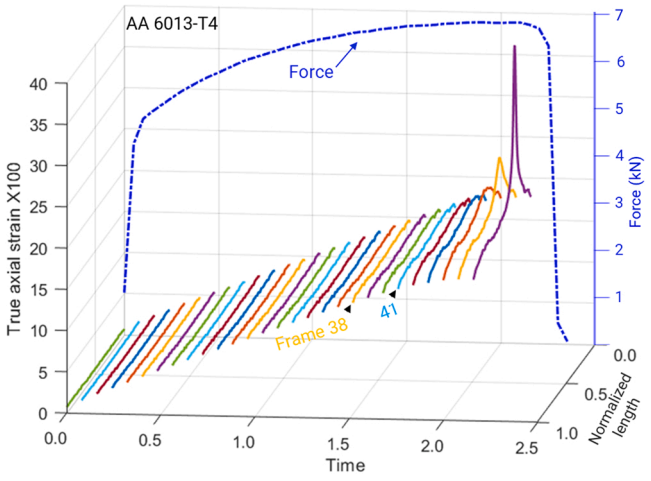

Fig. 9. – Three-dimensional plot showing the strain evolution along with the force-time curve during the UT test.

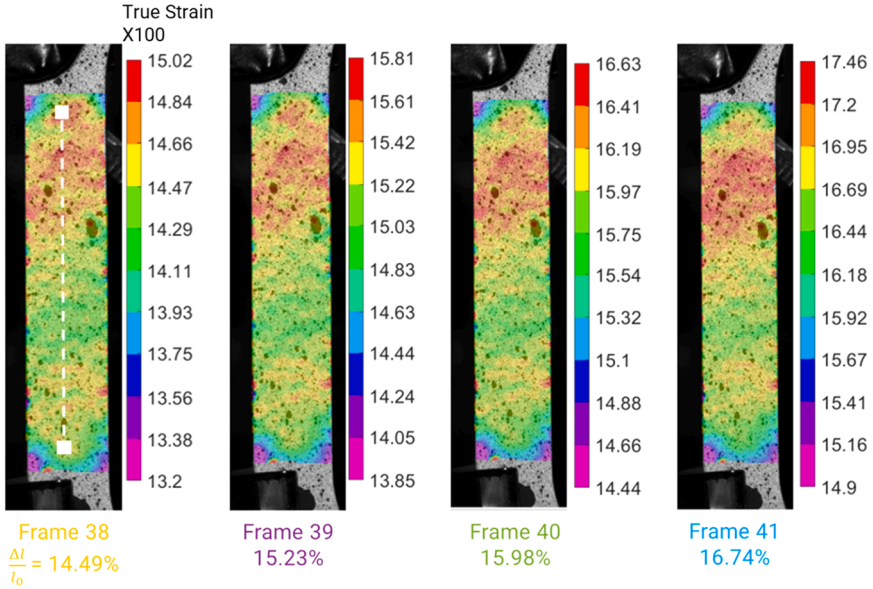

Fig. 7. – True strain fields on the surface of the UT specimen in frames between 38 and 41.

to experimentally observe a localization phenomenon before the force maximum as heterogeneity in strain rate field has been found before the maximum of the tensile force in some necking investigation studies by (Guelorget et al., 2006) and (Petit et al., 2014). This early localization phenomenon is examined by plotting strains from three different regions of the specimen as shown in Fig. 10a, which is the DIC frame just before fracture. An average of strains in the three regions identified in Fig. 10a, is plotted against time along with the force and the two AE signals as shown in Fig. 10b (with a zoomed in figure shown in Fig. 10c). As seen in the figures, strains in three regions increase uniformly until the peak in AE signal from the first sensor, before starting to deviate from one another with rapid increase in strain in the second region. This non-uniformity in strain is even more pronounced when plotting the strain-rate against time as shown in Fig. 11. The strain-rate from the three regions remains relatively constant until the first peak in the AE signal before deviating with a rapid acceleration of strain-rate in the second region. This confirms that the uniform strain field transitions to a non-uniform field before the force reaches its maximum, indicating the early onset of necking, which is well captured by the AE signals.

3. Circular cup drawing

3.1. Experimental setup

Cup drawing tests are performed on the double action hydraulic Greenerd press shown in Fig. 12 and described in detail by (Ha et al., 2020) and (Tian et al., 2016). A custom Marciniak-type punch (zoomed-in inset, Fig. 12) of 90 mm diameter is designed to house three AE sensors that will be used to triangulate the location of necking and fracture, which will occur for this geometry off the punch radius in the formed wall. The AE sensors are inserted into the punch face along with compression springs and insulating sleeves as shown in the punch CAD model in Fig. 13. The punch is attached to a hydraulic cylinder of 260 kN force capacity and 305 mm of stroke while the blank-holder is actuated

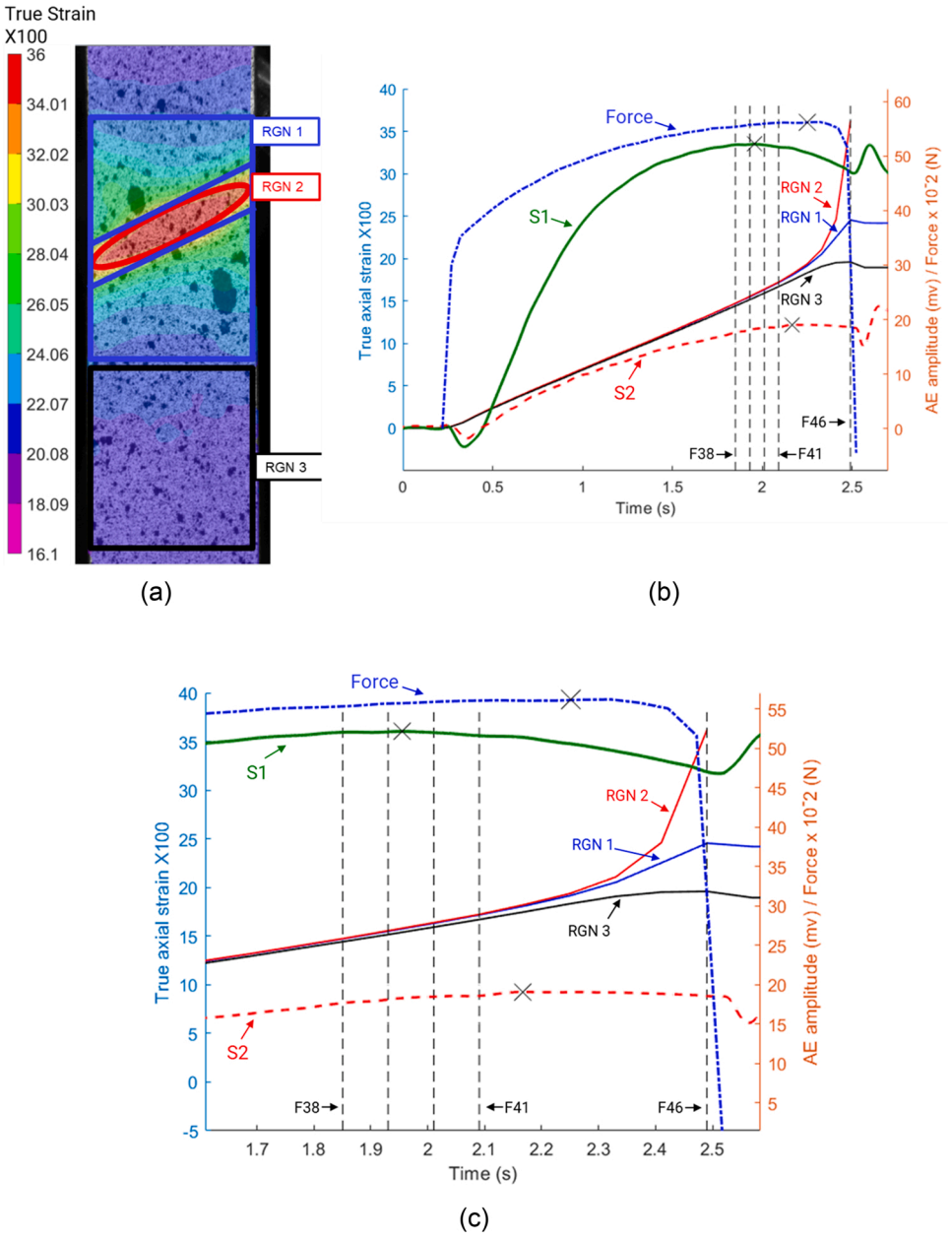

Fig. 10. – (a) DIC frame of the UT specimen just before fracture, showing three different regions of strain extraction, (b) plot of average strains and force vs time along with AE signals, and (c) zoomed in figure showing the regions of interest of the plot.

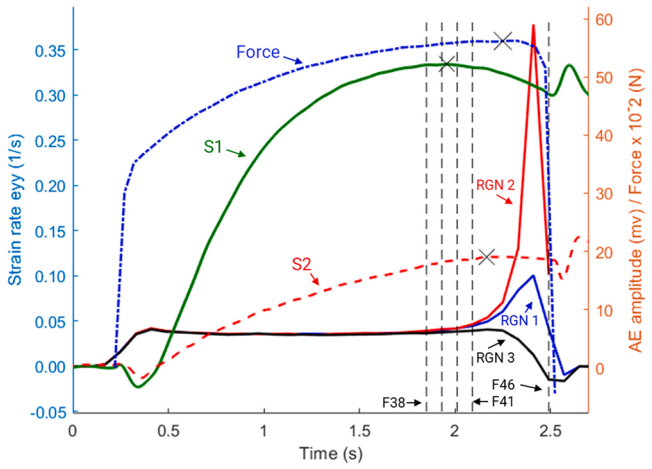

Fig. 11. – Plot of strain-rate and force vs time along with AE signals.

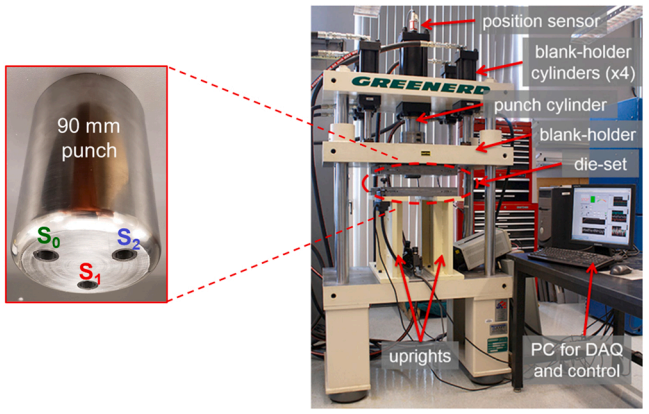

Fig. 12. – Experimental setup of cup drawing tests showing the press and the custom Marciniak-type punch designed to house three AE sensors.

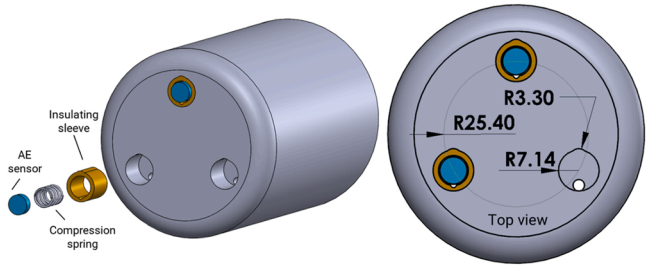

Fig. 13. – CAD model of the punch showing the details of AE sensor assembly including compression springs and insulating sleeves.

by 4 hydraulic cylinders of 112 kN force capacity each. A manifold with a relief valve and 5 proportional valves is used to connect the 5 hydraulic cylinders to a high-pressure hydraulic pump of 210 bar and 32 l/min capacity. A punch speed of 7.0 mm/s is used in the cup drawing tests. The system operates under open-loop control, with a constant opening of the proportional valve that controls the punch cylinder.

Square blanks with 195 mm sides are fabricated from the same stock of AA6013-T4 sheets as the uniaxial tension tests. During the tests, a lock ring of 150 mm diameter and 3 mm thickness (see Fig. 14) is used to prevent the drawing of the flange and promote the stretching of the blank. The blanks are generously lubricated before each experiment using the drawing lubricant Drawsol WM 4740. To control the fracture location around the circumference of the punch geometry, a rectangular

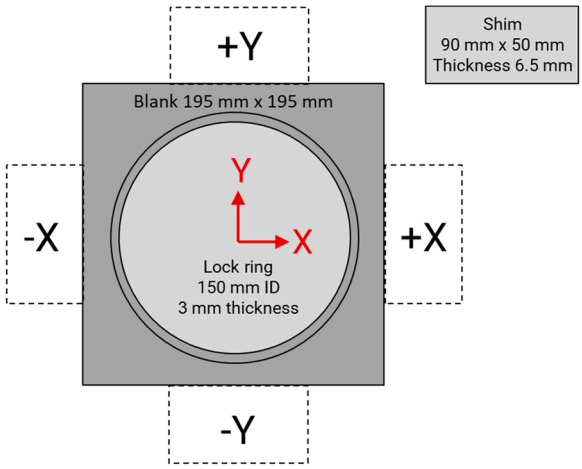

Fig. 14. – Experimental details and schematic of the blank, lock ring, and shim locations.

shim (i.e., piece of metal) of 90 mm by 50 mm with a 6.5 mm thickness is placed near the blank on one of the major axis directions, i.e., +X, -Y, -X and +Y. This prevents the binder plate from contacting the blank and forces the fracture to occur on the opposite side of the geometry where the material is constrained more in the lock ring, i.e., -X, +Y, +X, and –Y respectively. Details and a schematic of the blank, lock ring and shim locations are shown in Fig. 14.

3.2. Triangulation method

An experimental setup is implemented to record the elastic waves emitted from a source, by AE sensors positioned at different locations on a test specimen. Once the signals are received, a general triangulation technique is used, analyzing the arrival times of the signals at the different sensors to determine the source location. In this work, the triangulation method outlined in Tobias (1974, 1976) is implemented.

The AE sensors are positioned at the corners of an equilateral triangle within the punch, as shown in Fig. 15, with the origin for both Cartesian and polar coordinates at the reference sensor, S_0. The positions for three sensors can be defined as $S_0(0, 0)$, $S_1(x_1, y_1)$ and $S_2(x_2, y_2)$, with the AE

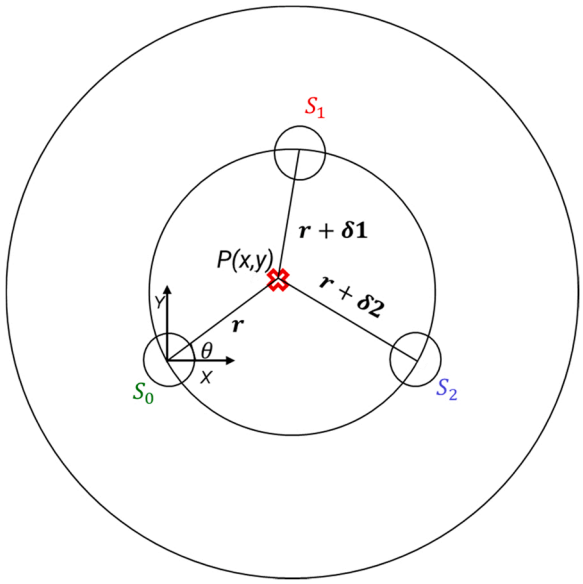

Fig. 15. – Position of AE sensors on the punch face for triangulation by time difference of arrival of signals.

source position as $P(x, y)$. A distance r from S_0 gives rise to path differences δ_1 and δ_2 defined by $\delta_1 = (PS_1) - (PS_0) = t_1 * v$ and $\delta_2 = (PS_2) - (PS_0) = t_2 * v$, where v is the velocity of the propagation, and t_1 and t_2 are the differences in arrival time measured for sensors S_0 and S_1, and S_0 and S_2, respectively. The AE source at P is located at the intersection of three circles with centers S_0, S_1, and S_2 and radii r, $r + \delta_1$, and $r + \delta_2$ respectively. The circles equations are given by:

$$\begin{aligned} x^2 + y^2 &= r^2 \\ (x - x_1)^2 + (y - y_1)^2 &= (r + \delta_1)^2 \\ (x - x_2)^2 + (y - y_2)^2 &= (r + \delta_2)^2 \end{aligned} \tag{1}$$

Rearranging the above equations and changing to polar coordinates (see Fig. 15) yields the general equation of form:

$$cos(\Theta - \Phi) = K \tag{2}$$

where,

$$K = \frac{A_2\delta_1 - A_1\delta_2}{B} \tag{3}$$

and

$$tan\Phi = \frac{(A_1 y_2 - A_2 y_1)}{(A_1 x_2 - A_2 x_1)} \tag{4}$$

In these equations,

$$B = \left[(A_1 x_2 - A_2 x_1)^2 + (A_1 y_2 - A_2 y_1)^2\right]^{\frac{1}{2}} \tag{5}$$

$$\begin{aligned} A_1 &= x_1^2 + y_1^2 - \delta_1^2 \\ A_2 &= x_2^2 + y_2^2 - \delta_2^2 \end{aligned} \tag{6}$$

If we introduce

$$\beta = cos^{-1}|K| \tag{7}$$

Then, the above equations are transformed into:

$$(\Theta - \Phi) = \beta + 2n\pi \;\; or \;\; -\beta + 2n\pi \quad for \;\; n = 0, \pm 1, \pm 2 \tag{8}$$

$$\Theta = (\alpha + \beta) + 2m\pi \;\; or \;\; (\alpha - \beta) + 2m\pi \quad for \; m = 0, \pm 1, \pm 2 \tag{9}$$

Eq. 9 gives general solutions with two possibilities for Θ in the range of $-\pi$ to $+\pi$. To resolve the ambiguous solutions, a fourth sensor can be placed at an arbitrary position, and the difference in arrival time measured by the fourth sensor with that calculated for the source location can be compared. In this work, only three sensors are used during the tests for simplicity of punch design and fabrication. Besides, for the cup drawing results shown in Section 3.3, the failure always happens at the punch radius and the triangulation method yields a unique solution.

This triangulation technique is verified using pencil lead break tests (Hsu, 1981) at different locations around the punch. Note that an AE wave, generated by breaking a pencil lead, is also known as a Hsu-Nielsen source. Results from one of the lead break tests on the punch are shown in Fig. 16, with the AE signal received by each of the three sensors plotted with respect to time. The signals are offset by + /- 0.1 V to see more clearly the arrival times marked as "x" (Fig. 16). In this test, the pencil lead breaks at $(r, \Theta) = (-18$ mm, $-180°)$ with the origin of the coordinate system placed at the center of the punch. Based on the time difference of arrival of signal to each sensor, the predicted location using the triangulation method above is $(r, \Theta) = (-17.9$ mm, $-178.7°)$, which is close to the actual source location. Similar results are obtained by breaking the pencil lead at different locations, verifying the validity of the adopted triangulation method.

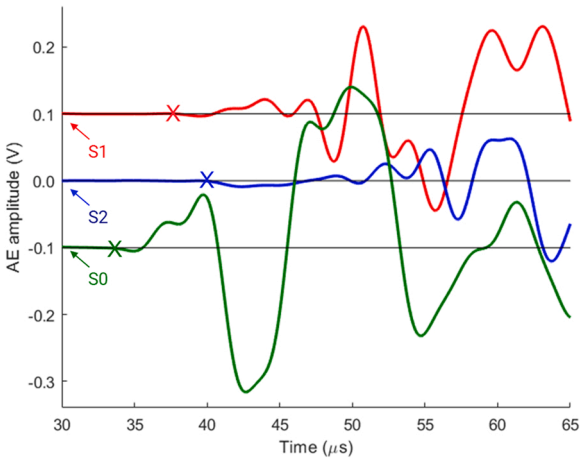

Fig. 16. – AE signals from a lead break test (Note the signals are offset by +/- 0.1 V for clarity).

3.3. Results

As described in Section 3.1, a custom punch with incorporated AE sensors and square aluminum blanks is used for the cup drawing tests. A total of 15 tests (i.e., 4 shim locations and one without shim, with three repetitions each) are performed with fractures intended along the four directions (+X, -Y, -X, and +Y) using the shim, and an uncontrolled fracture without a shim. The rolling direction of the sheet is positioned along the X direction during the tests. Only one representative test result (one of the shim positions at +X) is described in detail below, with the cumulative results summarized later in the section.

A cup drawing test result, i.e., the AE signals from the three sensors, for a shim placed at +X is shown in Fig. 17. The AE signals are filtered as described in Section 2.3. However, the data is not as smooth as the UT tests due to the test complexity caused by contact between the AE sensors and the specimen, and additional electrical noise during the test. However, like the UT tests described in Section 2.6, as the plastic deformation increases, the AE signal from each sensor increases as well, until it reaches a maximum, followed by a decrease in amplitude until the specimen fractures, as indicated by the spikes, i.e., burst signals, in Fig. 17. Similar to the uniaxial tension results with diffuse necking, the maxima in the AE signals appear to correspond to the early onset of localized necking. Based on the time differences of the AE peaks (marked as "x") in Fig. 17, the triangulation method described in Section 3.2 predicts the fracture location of $(r, \Theta) = (44.4$ mm, $173°)$. This prediction is close to the actual location of $(r, \Theta) = (45.0$ mm, $176°)$ observed

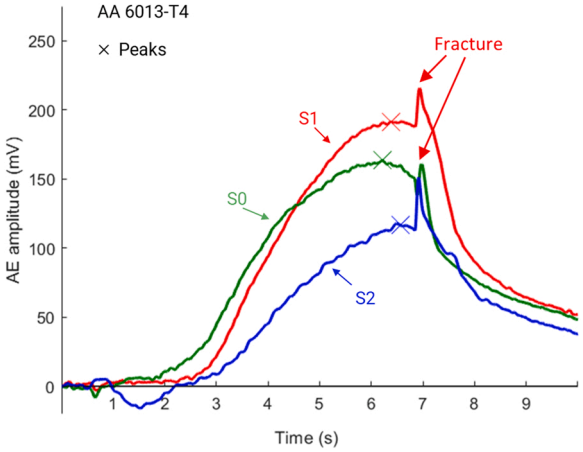

Fig. 17. – AE signals from a cup drawing test with shim placed at +X.

through DIC images, i.e., the region of maximum principal strain in the image just prior to fracture. Note, for easier reference, the origin of the coordinates is shifted to the center of the specimen and lined up with the major directions shown in Fig. 14.

The failed specimen from a cup drawing test with the shim placed at +X is shown in Fig. 18. The principal strain field at the onset of fracture from DIC is shown in Fig. 19. The predicted location by the triangulation method is marked as "x" in Fig. 19, which lies close to the observed necking and fracture location at the punch radius. As seen in Figs. 18 and 19, strain localization followed by fracture is observed in the -X direction, opposite to the location of the shim as expected. The strains from DIC are extracted from different locations near and outside of the localization region on the cup at the punch radius and face as marked in Fig. 19, i.e., P0 – P4. The strains are plotted along with the AE signal from one of the AE sensors (S_0) as shown in Fig. 20. The strain extracted near the localization region (i.e., P3 in Fig. 19) is higher than the strains at other locations. Furthermore, the strain at P3 increases rapidly as the plastic deformation approaches necking, followed by fracture. As was the case in the UT tests with diffuse necking, the AE amplitude peak seemingly corresponds to the early onset of localized necking as seen in Fig. 20. The principal strain field from DIC corresponding to the AE amplitude peak, indicating the early onset of necking is shown in Fig. 21.

Similar results are obtained when the shim is placed along -X, -Y and +Y directions, as well. The fracture location for the tests with the shim is always on the opposite side of the shim location. Alternatively, for the tests with no shim, the fracture could be anywhere along the punch radius. The predicted fracture locations from the triangulation method using the AE signals for all of the tests are found to be relatively close to the actual failed locations. The summary of all 15 test results showing the predicted fracture location is shown in Table 2. Though the process is sensitive to the accurate position of the blank placement, shim position, and uniform lubrication, the summarized results for repeated tests indicate that the localized necking location in cup drawing tests can be predicted before the fracture using the AE measurement techniques described in this paper. While the angles are not extremely precise, these would be sufficient to, e.g., decrease the binder force for the case of a standard servo press or tilt the binder away from the eminent necking location in the case of a 3D servo press described in (Chen et al., 2022) and (Groche et al., 2022). Note all the fracture locations are near the 45 mm punch radius, despite the fact that triangulation assumes a planar geometry, while the fractures occur off the punch radius. These results highlight the significant potential of using AE sensors to monitor for the early onset of necking and could be the required observer in a closed loop control scheme for the process to prevent material fracture during metal deformation.

Fig. 18. – Failed specimen from a cup drawing test with shim placed at +X.

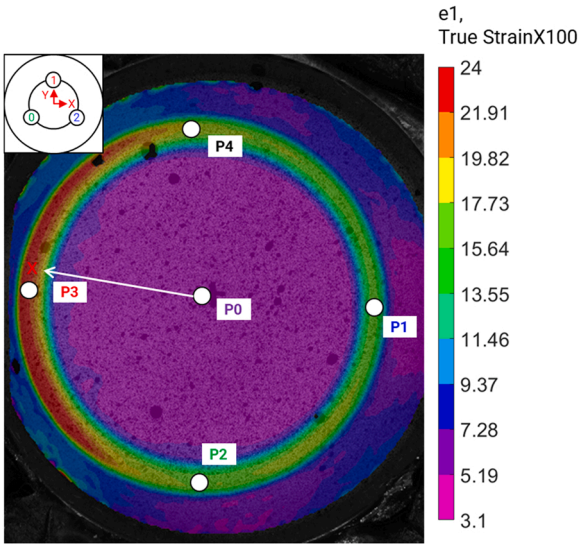

Fig. 19. – Strain field from DIC at the onset of fracture along with five locations for strain extractions.

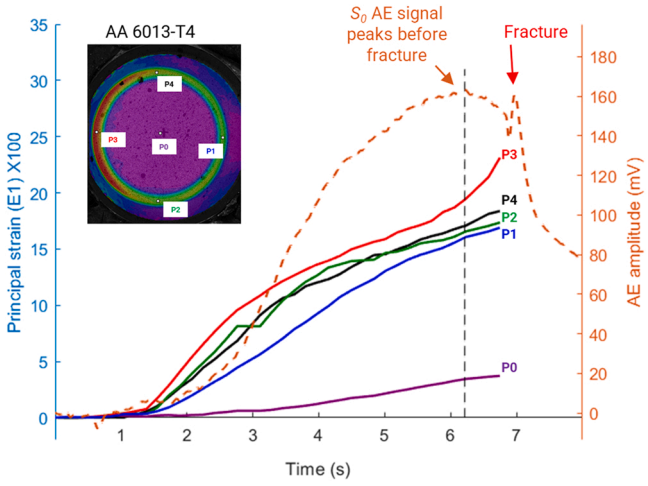

Fig. 20. – Plot of strains extracted from five locations along with AE signal from one of the sensors *(S0)*.

4. Discussion

4.1. Accuracy assessment

The results from the uniaxial tension tests consistently show that the AE signals peak when the uniform strain field starts to transition to a non-uniform field, indicating the early onset of diffuse necking. This indicates that the major source of the AE signal is dislocation activity, so that when localization sets-in, which implies elastic unloading of the majority of the specimen, the overall AE activity is reduced. The experimental data has some noise that is believed to be caused by tooling, friction, experimental setup, measurement apparatus, and some other random environmental noise. For example, Dunegan et al. (1968) showed that hydraulic grips are a source of noise that is captured by the AE sensors. It is believed that with a cleaner data set it is possible to increase the accuracy of predicting the early onset of necking. This may involve designing a better filter to process the signal, using sensors that have higher frequency response, improved experimental setup (e.g., an alternative to clamp the AE sensors, a better application of glycerin, etc.), or eliminating noise sources from the surroundings. Similarly, the same noise sources of the UT test are applicable to the cup drawing. In

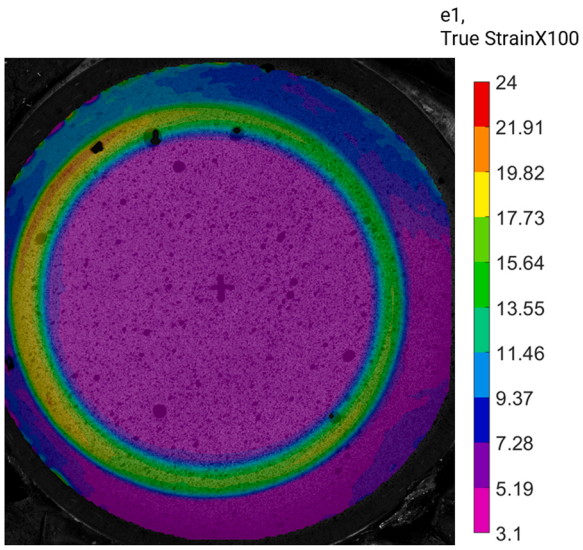

Fig. 21. – Strain field from DIC corresponding to the AE amplitude peak.

Table 2
Summary of results from 15 cup drawing tests.

Shim Location Fracture Location	Test #	Fracture Radius (mm)	Fracture Angle (deg.)	Difference in angle (Observation-Prediction)
Right (+X);	1	44.4	173	1
Anticipated at	2	43.8	167.8	4.2
± 180°	3	42.7	-161.6	1.4
Bottom (-Y);	1	41.8	88.1	1.9
Anticipated at	2	44.5	90.4	0.4
90°	3	42.2	100.4	2.6
Left (-X);	1	42.8	-17.1	9.9
Anticipated at	2	42.1	-52.8	9.8
0°	3	42.8	-12.6	9.4
Top (+Y);	1	43.4	-87.8	2.2
Anticipated at	2	42.4	-93.3	1.7
− 90°	3	43.5	-111.8	5.8
No Shim;	1	43.4	-100.5	9.5
Free	2	43.1	-147.8	2.8
	3	42.4	-134.5	6.8

addition to the noise sources mentioned above, in the real industrial forming conditions, there could be possible secondary sources of noise including electrical noise resulting from multiple electrical systems, machine vibrations, etc. Thus, eliminating or reducing those sources could result in an improved estimation of the fracture location in the cup drawing. Yet, with the presented results, the estimated fracture location is comparable to the actual values of cup drawing with reasonable error, so a cleaner signal might have only modest improvement on the results.

Lastly, the accuracy of predicting the failure location is also dependent on the AE peak velocity used. This was determined to be 115 mm/s from UT tests (see Section 2.6). With this estimate, the adopted triangulation method predicted fracture location in cup drawing tests with reasonable accuracy. The velocity parameter during triangulation is found to be more sensitive to the predicted radial location than the angular location. For instance, using a 5% higher velocity would increase the predicted radial location by 20% with almost no change in the predicted angular location.

4.2. Modeling of AE activity

As stated earlier, our current understanding is that dislocation activity is the primary source of AE activity. In order to support or refute this postulate, an analytical model that was proposed by Gilman (1966) is used. He expressed the mobile dislocation density as a function of plastic strain. The model has two parts: one that linearly increases the total dislocation density due to the regenerative process of dislocation creation, and another one that is the exponential decay in dislocation density due to the decrease in the dislocation mobility, e.g., due to pile-ups, formation of substructures, etc. Combined, these provide the total dislocation density with plastic strain, i.e.:

$$N_m = M\epsilon_p e^{-\phi\epsilon_p} \tag{10}$$

where, N_m= dislocation density (dislocation/m^2), M= dislocation multiplication coefficients (m^{-2}), ϵ_p= plastic strain, ϕ = constant (assumed to be the reciprocal of the plastic strain value at which the AE signal peaks).

Dunegan and Harris (1969) investigated the AE activity in a UT test of AA7075-T6 and found a perfect match with the dislocation density predicted by Gilman's model. It should be noted that this material has limited work-hardening and a uniform elongation of about 0.1. However, that finding did not hold valid for Iron-3% silicon, presumably due to the presence of Lüders strain along the specimen gauge length and the rate at which the plastic deformation happens. We applied Gilman's model to our results for one of the AE sensors from a uniaxial tension test, see Fig. 22. In the figure, the dislocation multiplication coefficient of aluminum, M, is taken as 80E10^9 cm^{-2} from Gilman (1966) and the plastic strain is obtained from DIC. The graph shows that the increase of the AE amplitude correlates very well with the increase in dislocation activity, substantiating the claim that the former is mainly driven by the latter, at least up to the maximum force (cf. Fig. 6a), where the deformation is essentially uniform inside the gage section. As a possible extension of this work, a quantitative microstructural and metallographic analyses could be performed to measure the dislocation activities during the tests. Dislocation densities can be measured through the direct method of Transmission Electron Microscopy (TEM) or indirect methods such as X-ray diffraction (XRD) and neutron diffraction techniques (Muiruri et al., 2020). These measurements can then be compared with the AE measurements to correlate AE activity and dislocations during plastic deformation.

4.3. Closing remarks

Despite all of the possible error sources that have been discussed, the results suggest that AE sensors can predict the onset of necking and could be potentially used in a closed loop control system in press-forming. The goal is to implement this technique in a 3D Servo Press to simultaneously monitor the cup drawing operation and adjust the process to improve sheet formability (Groche et al., 2022). In addition to

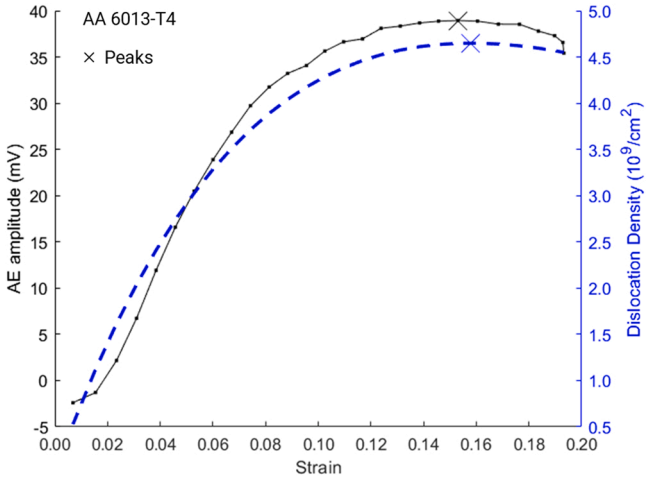

Fig. 22. – Plot of AE signal and dislocation density using Gilman's model.

a vertical ram motion, the 3D Servo Press has an additional two rotational degrees of freedom, which allow the press to move, e.g., with a full continuous orbital motion (Breunig et al., 2019) or tilting of the binder to allow more material to flow into the forming area. The overall aim is to implement a closed loop system that adjusts cup drawing parameters (e.g., pressure, angle, etc.) once necking is predicted by the AE system, to increase formability.

5. Conclusions and outlook

The early onset of necking was determined by analyzing the emitted elastic waves during UT tests of AA6013-T4. The AE signal measured by the custom piezoelectric sensors at the ends of the UT specimen gage length along with the surface strain from DIC revealed that the maximum amplitude of the AE signal corresponds to a diffuse necking, which initiates before the maximum force is attained by the specimen. The AE signal peak velocity was determined based on the time difference in the signal arrival and the fracture location along the gage length of the specimen. Similarly, the AE technique was employed to accurately predict the necking and fracture location in a cup drawing process using time difference of arrival of the AE signals and triangulation. The position of strain localization was controlled by the addition of a shim in the process. Again, the peak of the AE signal corresponded to the onset of necking prior to the subsequent failure of the specimen.

The AE technique implemented in this work could be used in the design of a closed loop control system, which monitors the onset of necking in forming operations. The results show that the onset of necking and the peak of an AE signal are correlated. This can be used as an indication of the eminent fracture, which typically occurs soon afterwards. For the presented cup drawing results, the time difference between the first sensor peak and fracture is between 0.3 and 0.9 s, which poses a challenge in implementing a plausible control scheme considering the sampling time, filtering, location estimation and actuation. At the same time, these tests were conducted at relatively high punch speed of 7 mm/s, giving possibility that conducting tests at slower speed could provide ample time to implement a feasible control scheme. However, a slower punch speed increases production time in an industrial process and may not be economically beneficial. Thus, a dedicated circuit could be designed in lieu of a digital filter to implement an efficient and relatively faster control system in an actual industrial process. In addition, as opposed to waiting until the peak of the AE signal, i.e. zero-slope, a user-defined threshold in terms of change in slope of AE signal could be used to predict the onset of necking, and implemented in a controller that adjusts the process parameters to improve formability.

CRediT authorship contribution statement

Madhav Baral: Conceptualization, Methodology, Software, Formal analysis, Visualization, Investigation, Data curation, Writing – original draft, Writing – review & editing, Supervision. **Ali-Al Jewad:** Methodology, Formal analysis, Visualization, Investigation, Data curation, Writing – original draft, Writing – review & editing. **Alexander Breunig:** Conceptualization, Writing – review & editing. **Peter Groche:** Conceptualization, Writing – review & editing, Supervision, Funding acquisition. **Jinjin Ha:** Conceptualization, Writing – review & editing, Supervision. **Yannis P. Korkolis:** Conceptualization, Visualization, Writing – review & editing, Supervision, Funding acquisition. **Brad Kinsey:** Conceptualization, Methodology, Visualization, Data curation, Project administration, Writing – review & editing, Supervision, Funding acquisition.

Declaration of Competing Interest

The authors declare that they have no known competing financial interests or personal relationships that could have appeared to influence the work reported in this paper.

Data availability

Data will be made available on request.

Acknowledgements

This research was supported by NSF award CMMI-1727490 and DFG award 386415239. This support is acknowledged with thanks.

References

Barschdorff, D., Haupt, H., 2000. Monitoring of Metal Forming by Acoustic Emission. XVI IMEKO World Congr. Wien.

Behrens, B.A., El-Galy, I., Huinink, T., Buse, C., 2011. Online monitoring of deep drawing process by application of acoustic emission. In: Special Edition: 10th International Conference on Technology of Plasticity, 2011. ICTP, pp. 385–389.

Berneder, J., Prillhofer, R., Enser, J., Schulz, P., Melzer, C., 2011. Study of the artificial aging kinetics of different AA6013-T4 heat treatment conditions. Suppl. Proc.: Mater. Fabr., Prop., Charact., Model. 321–328. https://doi.org/10.1002/9781118062142.ch39.

Breunig, A., Hoppe, F., Groche, P., 2019. Localized blank-holder pressure control in cup drawing through tilting of the ram. In: Proeedings of NUMIFORM, pp. 583–586.

Calabrese, L., Proverbio, E., 2020. A Review on the Applications of Acoustic Emission Technique in the Study of Stress Corrosion Cracking. Corros. Mater. Degrad. 2021, Vol. 2, Pages 1–30 2, 1–30. https://doi.org/10.3390/CMD2010001.

Carpenter, S.H., Higgins, F.P., 1977. Sources of acoustic emission generated during the plastic deformation of 7075 aluminum alloy. Met. Trans. A 8 A 1629–1632. https://doi.org/10.1007/BF02644869.

Chen, K., Breunig, A., Ha, J., Kinsey, B.L., Groche, P., Korkolis, Y.P., 2022. Robustness of deep-drawing finite-element simulations to process variations. Int. J. Mater. Form. 2022 153 15, 1–17. https://doi.org/10.1007/S12289-022-01695-3.

Considère, M., 1885. Memoire sur l'emploi du fer et de l'acier dans les constructions. Vue Ch. Dunod.

Dunegan, H., Harris, D., 1969. Acoustic emission-a new nondestructive testing tool. Ultrasonics 7, 160–166. https://doi.org/10.1016/0041-624X(69)90660-X.

Dunegan, H.L., Harris, D.O., Tatro, C.A., 1968. Fracture analysis by use of acoustic emission. Eng. Fract. Mech. 1, 105–122. https://doi.org/10.1016/0013-7944(68)90018-0.

Fisher, R.M., Lally, J.S., 1967. Microplasticity detected by an acoustic technique. Can. J. Phys. 45, 1147–1159. https://doi.org/10.1139/p67-084.

Fitzgerald, E.R., 2005. Mechanical resonance dispersion and plastic flow in crystalline solids. J. Acoust. Soc. Am. 32, 1270. https://doi.org/10.1121/1.1907894.

Gilman, J.J., 1966. Progress in the microdynamical theory of plasticity. Proc. 5th Natl. Congr. Appl. Mech. ASME 385–403.

Groche, P., Breunig, A., Chen, K., Molitor, D.A., Ha, J., Kinsey, B.L., Korkolis, Y.P., 2022. Effectiveness of different closed-loop control strategies for deep drawing on single-acting 3D Servo Presses. CIRP Ann. https://doi.org/10.1016/J.CIRP.2022.04.072.

Guelorget, B., François, M., Vial-Edwards, C., Montay, G., Daniel, L., Lu, J., 2006. Strain rate measurement by electronic speckle pattern interferometry: a new look at the strain localization onset. Mater. Sci. Eng. A 415, 234–241. https://doi.org/10.1016/J.MSEA.2005.09.090.

Gupta, R., Mitchell, D., Blanche, J., Harper, S., Tang, W., Pancholi, K., Baines, L., Bucknall, D.G., Flynn, D., 2021. A Review of Sensing Technologies for Non-Destructive Evaluation of Structural Composite Materials. J. Compos. Sci. 2021, Vol. 5, Page 319 5, 319. https://doi.org/10.3390/JCS5120319.

Ha, J., Baral, M., Korkolis, Y.P., 2018. Plastic anisotropy and ductile fracture of bake-hardened AA6013 aluminum sheet. Int. J. Solids Struct. 155, 123–139. https://doi.org/10.1016/j.ijsolstr.2018.07.015.

Ha, J., Coppieters, S., Korkolis, Y.P., 2020. On the expansion of a circular hole in an orthotropic elastoplastic thin sheet. Int. J. Mech. Sci. 182, 105706.

Hao, S., Ramalingam, S., Klamecki, B.E., 2000. Acoustic emission monitoring of sheet metal forming: characterization of the transducer, the work material and the process. J. Mater. Process. Technol. 101, 124–136. https://doi.org/10.1016/S0924-0136(00)00441-6.

Heiple, C.R., Carpenter, S.H., 1987. Acoustic emission produced by deformation of metals and alloys. J. Acoust. Em. 6, 177.

Hill, R., Hutchinson, J.W., 1975. Bifurcation phenomena in the plane tension test. J. Mech. Phys. Solids 23, 239–264. https://doi.org/10.1016/0022-5096(75)90027-7.

Hsu, N.N., 1981. Characterization and calibration of acoustic emission sensors. Mater. Eval. 39, 60–68.

Huang, J.Q., 2013. Non-destructive evaluation (NDE) of composites: acoustic emission (AE). Non-Destructive Eval. Polym. Matrix Compos. Tech. Appl. 12–32. https://doi.org/10.1533/9780857093554.1.12.

Huang, M., Jiang, L., Liaw, P.K., Brooks, C.R., Seeley, R., Klarstrom, D.L., 1998. Using acoustic emission in fatigue and fracture materials research. Jom 50, 1–14.

Hutchinson, J.W., Miles, J.P., 1974. Bifurcation analysis of the onset of necking in an elastic/plastic cylinder under uniaxial tension. J. Mech. Phys. Solids 22, 61–71. https://doi.org/10.1016/0022-5096(74)90014-3.

Jayakumar, T., Mukhopadhyay, C.K., Venugopal, S., Mannan, S.L., Raj, B., 2005. A review of the application of acoustic emission techniques for monitoring forming and grinding processes. J. Mater. Process. Technol. 159, 48–61. https://doi.org/10.1016/J.JMATPROTEC.2004.01.034.

Jemielniak, K., Otman, O., 1998. Tool failure detection based on analysis of acoustic emission signals. J. Mater. Process. Technol. 76, 192–197. https://doi.org/10.1016/S0924-0136(97)00379-8.
Kawamoto, S., Williams, R.S., 2002. Acoustic emission and acousto-ultrasonic techniques for wood and wood-based composites. Gen. Tech. Rep. 1–16.
Khalil, I.M.E.G., 2011. Application of Acoustic Emission and Signal Analysis Techniques in Monitoring Die Forging Processes of Light Alloys. PZH Produktionstechnisches Zent.
Kim, B.S., 1983a. Punch press monitoring with acoustic emission (AE) Part I: signal characterization and stock hardness effects. J. Eng. Mater. Technol. 105, 295–300. https://doi.org/10.1115/1.3225661.
Kim, B.S., 1983b. Punch press monitoring with acoustic emission (AE) Part II: effects of process variables. J. Eng. Mater. Technol. 105, 301–306. https://doi.org/10.1115/1.3225662.
Liang, S.Y., Dornfeld, D.A., 1990. Characterization of sheet metal forming using acoustic emission. J. Eng. Mater. Technol. 112, 44–51. https://doi.org/10.1115/1.2903185.
Luis, J., Chacon, F., 2015. Fault detection in rotating machinery using acoustic emission. Brunel University London.
Martínez-Donaire, A.J., García-Lomas, F.J., Vallellano, C., 2014. New approaches to detect the onset of localised necking in sheets under through-thickness strain gradients. Mater. Des. 57, 135–145. https://doi.org/10.1016/J.MATDES.2014.01.012.
Min, J., Stoughton, T.B., Carsley, J.E., Lin, J., 2017. A method of detecting the onset of localized necking based on surface geometry measurements. Exp. Mech. 57, 521–535. https://doi.org/10.1007/s11340-016-0232-4.
Mokbel, A.A., Maksoud, T.M.A., 2000. Monitoring of the condition of diamond grinding wheels using acoustic emission technique. J. Mater. Process. Technol. 101, 292–297. https://doi.org/10.1016/S0924-0136(00)00433-7.
Muiruri, A., Maringa, M., du Preez, W., 2020. Evaluation of dislocation densities in various microstructures of additively manufactured Ti6Al4V (Eli) by the method of X-ray diffraction. Materials 13, 1–23. https://doi.org/10.3390/MA13235355.
Nair, A., Cai, C.S., 2010. Acoustic emission monitoring of bridges: review and case studies. Eng. Struct. 32, 1704–1714. https://doi.org/10.1016/J.ENGSTRUCT.2010.02.020.
Nakao, Y., Dornfeld, D.A., 2003. Diamond turning using position and AE dual feedback control system. Precis. Eng. 27, 117–124. https://doi.org/10.1016/S0141-6359(02)00189-7.
Petit, J., Montay, G., François, M., 2014. Strain rate measurements by speckle interferometry for necking investigation in stainless steel. Int. J. Solids Struct. 51, 540–550. https://doi.org/10.1016/J.IJSOLSTR.2013.10.029.
Schofield, B.H., 1958. Acoustic Emission Under Applied Stress. Technical report. Wright Air Dev. Cent.
Selesnick, I.W., Sidney Burrus, C., 1998. Generalized digital butterworth filter design. IEEE Trans. Signal Process 46, 1688–1694. https://doi.org/10.1109/78.678493.
Sharpe, W.N., 2009. Springer handbook of experimental solid mechanics. Springer,.
Shukla, A., Dally, J.W., 2010. Experimental Solid Mechanics. College House Enterprises, Knoxville, TN.
Skåre, T., Thilderkvist, P., Ståhl, J.E., 1998. Monitoring of friction processes by the means of acoustic emission measurements—deep drawing of sheet metal. J. Mater. Process. Technol. 80–81, 263–272. https://doi.org/10.1016/S0924-0136(98)00130-7.
Tian, H., Brownell, B., Baral, M., Korkolis, Y.P., 2016. Earing in cup-drawing of anisotropic Al-6022-T4 sheets. Int. J. Mater. Form. https://doi.org/10.1007/s12289-016-1282-y.
Tobias, A., 1974. ACEMAN-a PDP 11 operating system for acoustic emission analysis. CEGB Berkeley Nucl. Lab. Rep. RD/B 3188.
Vacher, P., Haddad, A., Arrieux, R., 1999. Determination of the forming limit diagrams using image analysis by the corelation method. CIRP Ann. 48, 227–230. https://doi.org/10.1016/S0007-8506(07)63171-0.
Vanniamparambil, P.A., Guclu, U., Kontsos, A., 2015. Identification of crack initiation in aluminum alloys using acoustic emission. Exp. Mech. 55, 837–850. https://doi.org/10.1007/S11340-015-9984-5/FIGURES/15.
Wang, K., Carsley, J.E., He, B., Li, J., Zhang, L., 2014. Measuring forming limit strains with digital image correlation analysis. J. Mater. Process. Technol. 214, 1120–1130. https://doi.org/10.1016/J.JMATPROTEC.2014.01.001.